# Temperature Sensors Based on Negative Temperature Coefficient of ZnO Thin Films

Juan Jia, Hongxi Zhu, Wei Liu, Binghui Li, Zengliang Shi, Qiannan Cui, and Chunxiang Xu

***Abstract*— Based on the experimental discovery about the negative temperature coefficient (NTC) of ZnO, we fabricated a low-temperature sensor with ZnO thin film. Oxygen plasma and annealing treatment were carried out to manipulate the related defects and explore the negative temperature response, while a series of microstructural and optical properties were also characterized and compared for the cases before and after treatment. It demonstrated that zinc interstitials ($Zn_i$) played an important role in NTC response process. Moreover, we simulated the application conditions of cell cryopreservation and conducted relevant tests in the common temperature range of −120 °C–0 °C. The ZnO NTC sensor was applied for actual real-time temperature monitoring in a commercial low-temperature system. The sensor presented a nice sensitivity of $3.51 \times 10^4$ $\Omega \cdot K^{-1}$ at 90 K, a good repeatability, recoverability, and a fast response speed. The results showed a great potential of ZnO NTC sensor for biomedical cryogenics applications.**

***Index Terms*— Defect manipulation, low-temperature sensing, negative temperature coefficient, ZnO thin film.**

## I. Introduction

CRYOGENIC technology has important applications in space exploration, superconducting technology, and biomedical cryopreservation [1], [2]. It is scientific to explore some novel materials and devices with high performance for low-temperature sensing. So far, various low-temperature sensors have been developed, such as platinum resistance, diode thermometers, optical fiber sensor, and negative temperature coefficient (NTC) thermistors [2], [3], [4], [5]. However, they still suffer more or less shortcomings of complex structure, high cost, and narrow measurement range, and some of them are susceptible to electromagnetic interference [6], [7], [8].

NTC thermistors exhibit a decreased resistance as temperature increasing. Compared with other temperature sensors, this kind of thermistors is generally sensitive in the range of 1.5–300 K and strongly resistant to electromagnetic interference [9]. The traditional NTC thermistors are composed of several transition metal oxides, such as CoO, NiO, and MnO [10], [11]. It is assumed that the impurities and defects in the materials have influence on conductivity and NTC properties due to thermal activation mechanism. Thus, they are normally doped or compounded with elements and materials to improve the stability and sensitivity. However, the traditional NTC thermistors were normally composed of complex components with a specific ratio. For instance, the $Mn_{1.95-x}$–$Ni_{0.45}$–$Co_{0.15}$–$Cu_{0.45}$–$Zn_xO_4$ NTC thermistor was reported by adjusting the proportion ($x$) to improve its thermal stability, so the process of fabrication is inconvenient [12]. The physical mechanism of NTC response is mainly attributed to the charge transfer between adjacent ions of different valence elements in the crystal structure under the excitation of thermal energy. In addition, when the material is heated, the defects are excited as charge carriers to migrate within the material, thereby improving the conductivity, that is, the electron transition model between variable valence ions and the migration of internal defects in materials. Therefore, defects play an important role in NTC temperature sensing.

As a wide bandgap II–VI compound semiconductor oxide, the temperature-dependent optical and electrical properties of ZnO have been demonstrated by advanced researches, including several works on its NTC sensing in the temperature range of −193 °C–100 °C [13], [14], [15], [16], [17]. The intrinsic defects have a great effect on the conductivity of ZnO, which indicates the necessity of understanding the defect influence on NTC characteristics [18], [19], [20]. Therefore, it is significant to investigate the defect-related NTC response for advancing the development of ZnO low-temperature sensing.

In present work, we fabricated a simple-structured low-temperature sensor based on a ZnO thin film with high crystal quality. The measured current–voltage ($I$–$V$) curves in the

Manuscript received 24 March 2023; revised 6 August 2023; accepted 5 September 2023. Date of publication 2 October 2023; date of current version 24 October 2023. This work was supported in part by the National Natural Science of China under Grant 62075041 and Grant 61821002 and in part by the Fundamental Research Funds for the Central Universities in China under Grant 2242021k10009. The review of this article was arranged by Editor W. S. Kim. *(Juan Jia and Hongxi Zhu contributed equally to this work.) (Corresponding author: Chunxiang Xu.)*

Juan Jia, Hongxi Zhu, Zengliang Shi, Qiannan Cui, and Chunxiang Xu are with the State Key Laboratory of Bioelectronics, School of Biological Sciences and Medical Engineering, School of Physics, Southeast University, Nanjing 210096, China (e-mail: xcxseu@seu.edu.cn).

Wei Liu is with the College of Optical, Mechanical and Electrical Engineering, Zhejiang A&F University, Hangzhou 311300, China (e-mail: liuwei@zafu.edu.cn).

Binghui Li is with the State Key Laboratory of Luminescence and Applications, Changchun Institute of Optics, Fine Mechanics and Physics, Chinese Academy of Sciences, Changchun 130033, China (e-mail: binghuili@163.com).

Color versions of one or more figures in this article are available at https://doi.org/10.1109/TED.2023.3314400.

Digital Object Identifier 10.1109/TED.2023.3314400

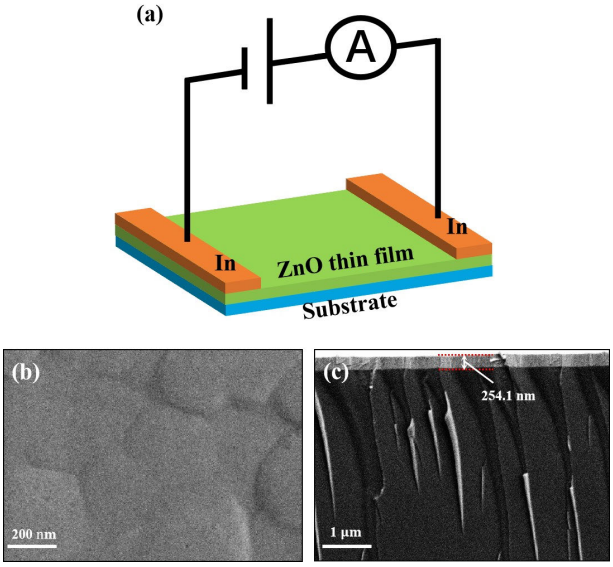


Fig. 1. (a) Schematic of ZnO thin-film sensor; *I–V* curves of ZnO sensor measured from 90 to 300 K. (b) Surface SEM photographs of MBE epitaxial ZnO films. (c) Cross-sectional SEM photographs of MBE epitaxial ZnO films.

range of 90–300 K showed a clear NTC characteristic. Oxygen plasma and annealing treatment were carried out to manipulate defects and catch their effect on NTC response. Then, X-ray diffraction (XRD) studies, photoluminescence (PL) spectra, and time-resolved PL (TRPL) were conducted to investigate the correlation between the defects and NTC response. Raman spectra, X-ray photoelectron spectroscopy (XPS), and temperature-dependent PL were characterized to analyze the mechanism of defect-related NTC properties. Moreover, we constructed the application scenario of cell cryopreservation based on the requirement in biomedical cryogenics, and relevant tests for the real-time low-temperature monitoring were conducted in the range of −120 °C–0 °C, which presented the feasibility, repeatability, and a fast response speed of the ZnO NTC sensor. It proved that ZnO NTC sensor is potential in biomedical cryogenics, such as cryotherapy, samples cryopreservation, and transportation.

## II. Experiment

### A. Materials and Fabrication of ZnO Sensors

The n-type ZnO thin films were grown on sapphire by molecular beam epitaxy (MBE) technique according to the previous work reported by He et al. [21]. For investigating the electrical properties, we used indium to fabricate electrodes at the ends of a slide ZnO thin film, as shown in Fig. 1(a). The temperature-dependent *I–V* characterizations were conducted with the temperature controller (Instec mK2000) and high-precision power source (KEYSIGHT B2961A). In order to study the factors affecting the NTC response, two experiments that can manipulate the defect states of ZnO were carried out. ZnO thin films were treated by oxygen plasma for 10 min with 100 W and annealed at 750 °C in $O_2$ for 1 h, respectively.

### B. Characterization of Materials and Devices

To explore the correlation between the defects and NTC response, relevant experiments were performed. The surface and cross-sectional morphology of the films were taken with a scanning electron microscope (SEM; Zeiss Ultra Plus). XRD was measured by a Rigaku Smartlab 3 KW x-ray diffractometer with Cu K$\alpha$ ($\lambda = 1.5418$ Å) as the radiation source. PL was measured by a homemade confocal microphotoluminescence setup using an Olympus BX35 microscope, excited by a 325-nm femtosecond pulsed laser with 10× objective. TRPL spectra were collected in an Optronis Optoscope sc-10 streak camera excited by a femtosecond pulsed laser (325-nm excitation wavelength, 100-fs pulsed duration, and 1-kHz repetition rate) as a signal detector and an excitation source. Raman spectra were captured using a 532-nm laser (Renishaw inVia spectrometer). The surface electronic states of ZnO thin film were analyzed by an XPS (Thermo Scientific Escalab 250Xi).

## III. Results and Discussion

### A. Structure and Morphology

Fig. 1(b) shows the surface SEM photographs of MBE epitaxial ZnO films. Well-grown ZnO thin films that are evenly distributed with a high density can be observed on the surface of the substrate. It can also be seen from the figure that the surface of ZnO thin films grown by MBE is relatively flat. Fig. 1(c) displays the cross-sectional SEM photograph of MBE epitaxial ZnO films and exhibits almost the same thickness of the thin films, which is about 254.1 nm.

### B. NTC Properties of ZnO Thin Film

To investigate the temperature sensing properties with NTC response, *I–V* characteristics were measured on the fabricated ZnO thin-film sensor. Fig. 2(a) shows the *I–V* curves from 90 to 300 K. The results exhibit an obvious symmetry and linearity, which means that the sensor has a good ohmic characteristic. The obtained temperature-dependent resistance (*R–T*) curve was shown in Fig. 2(b). It can be seen that the resistance decreases with the increasing temperature, which indicates an NTC response of ZnO sensor. The data were fitted by Boltzmann function, and the results of fitting reached $R^2 = 0.984$. It assumed that NTC properties are related to the distribution of electrons at each energy level. Therefore, oxygen plasma and annealing treatment were, respectively, carried out to study the influence of the defects on NTC response of ZnO sensor.

First, oxygen plasma treatment was conducted to manipulate defects. Fig. 3(a) presents the *R–T* curves of ZnO thin film by oxygen plasma treatment. The results of Boltzmann fitting reached $R^2 = 0.990$. It can be seen that NTC response before oxygen plasma treatment is more obvious. To further confirm the temperature sensing properties, the absolute sensitivity ($S$) and relative sensitivity ($W$) were calculated according to the mathematical definition of sensitivity [22], [23]

$$S = d_R/d_T$$
$$W = S * (T/R)$$

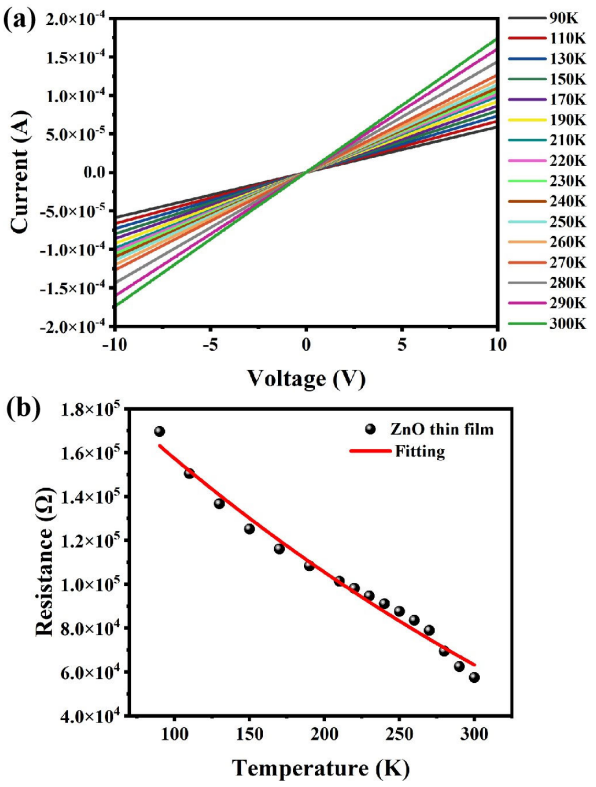


Fig. 2. (a) *I–V* curves of ZnO sensor measured from 90 to 300 K. (b) Temperature-dependent resistance from 90 to 300 K.

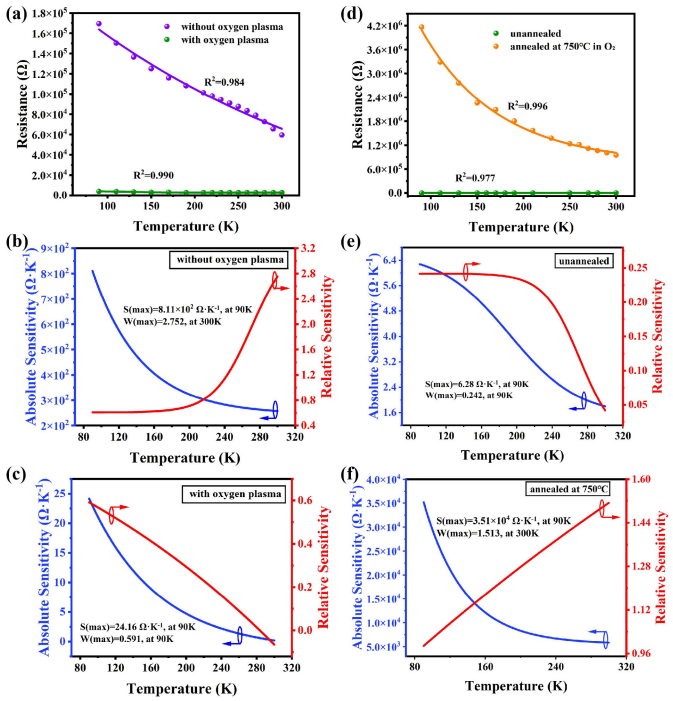


Fig. 3. (a) Temperature-dependent resistance from 90 to 300 K by oxygen plasma treatment; *S* and *W* curves (b) before and (c) after oxygen plasma treatment. (d) Temperature-dependent resistance from 90 to 300 K by annealing; *S* and *W* curves (e) before and (f) after annealing.

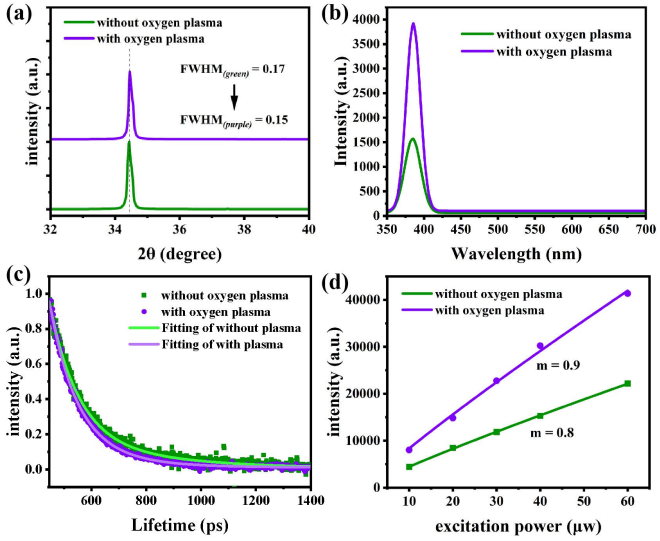


Fig. 4. Oxygen plasma treatment. (a) XRD pattern. (b) Room-temperature PL. (c) TRPL decay at 325 nm. (d) Variation of PL integrated intensity with the increasing of excitation power.

where $R$ is the resistance of ZnO thin film at $T$ temperature and $T$ is the Kelvin temperature. In Fig. 3(b), ZnO sensor had an $S$(max) of 8.11 × $10^2$ Ω·$K^{-1}$ at 90 K and a $W$(max) of 2.752 at 300 K before oxygen plasma treatment. As shown in Fig. 3(c), $S$(max) dropped by about 30 times to 24.16 Ω·$K^{-1}$ at 90 K and $W$(max) became 0.591 at 90 K after oxygen plasma treatment. It showed that NTC response of ZnO sensor became worse after oxygen plasma treatment.

To further investigate the effect of defects on NTC properties, annealing treatment was performed at 750 °C. Fig. 3(d) shows the $R$–$T$ results of ZnO sensor by annealing treatment and the data conformed to the Boltzmann distribution as well. The fitting of unannealed sample was $R^2$ = 0.977 and ZnO thin film annealed at 750 °C was with $R^2$ = 0.996. An enhancement of NTC responsivity can be observed after annealing. As shown in Fig. 3(e), $S$(max) was 6.28 Ω·$K^{-1}$ at 90 K and $W$(max) was 0.242 at 90 K before annealing. In Fig. 3(f), $S$(max) raised nearly four orders of magnitude to 3.51 × $10^4$ Ω·$K^{-1}$ at 90 K and $W$(max) increased to 1.513 at 300 K for annealed sample. Obviously, the fabricated ZnO sensor after annealing had a higher NTC sensitivity.

### C. Mechanism of Defect-Dependent NTC Response

A series of characterizations were conducted on the samples to explore the influencing factors on NTC response. Fig. 4(a) displays the XRD pattern of ZnO thin film by oxygen plasma treatment. A well-defined diffraction peak was observed about $2\theta$ = 34.5°, corresponding to the (002) plane. Meanwhile, it can be found that the full-width at half-maximum (FWHM) value decreased from 0.17° to 0.15°. The PL spectra at the same excitation position are shown in Fig. 4(b). The only peak was found around 385 nm, which is the intrinsic peak of ZnO thin film, indicating that ZnO thin film grown by MBE can be used as standard samples for subsequent defect analysis. Moreover, an evident increase in emission intensity was found. It can be explained that surface defects were passivated after oxygen plasma treatment. In Fig. 4(c), the TRPL decay results

TABLE I
ROOM-TEMPERATURE TRPL DECAY FITTING RESULTS

| Sample | τ1/ps | τ2/ps | ετ2 |
|---|---|---|---|
| without oxygen plasma | 103 | 375 | 0.03 |
| with oxygen plasma | 94 | 188 | 0.05 |
| unannealed | 102 | 226 | 0.34 |
| annealed at 750 °C | 93 | 243 | 0.13 |

were fitted by the double exponential model

$$I = A_1 \exp(-t/\tau_1) + A_2 \exp(-t/\tau_2) + I_0.$$

It suggested two distinct luminescence processes. Table I summarizes the decay times obtained by fitting, where $\tau_1$ is the fast decay component of free photo-generated carriers and $\tau_2$ is the slow decay of the electron recapturing and nonradiative recombination processes [24], [25]. We can see that both $\tau_1$ and $\tau_2$ decreased after oxygen plasma treatment. It is shown that the nonradiation recombination of shallow-level surface defects was relatively weakened. The luminescence weight value for long lifetime $\varepsilon_{\tau 2}$ was calculated according to the following formula [26]

$$\varepsilon_{\tau_2} = A_2\tau_2/(A_1\tau_1 + A_2\tau_2).$$

It can be found that $\varepsilon_{\tau 2}$ increases, which is attributed to the improvement of surface defects after oxygen plasma treatment. Fig. 4(d) shows the integrated PL intensities ($I$) at different excitation power densities ($P$). The relationship between the integrated intensity and the excitation power density can be fitted in power exponent [27]

$$I \sim cP^m$$

where $c$ is a coefficient and $m$ is an evaluation index of the constitution of free-to-bound recombination on the light emission process. The value of $m$ after oxygen plasma treatment was increased from 0.8 to 0.9, indicating that the free exciton emission became significant while bound-exciton emission due to defects and impurities was relatively reduced. This further supports that the defect concentration was reduced after oxygen plasma treatment.

In Fig. 5(a), the FWHM of XRD spectra broadened from 0.17° to 0.20°, which indicates that the crystal quality degraded after annealing at 750 °C. As shown in Fig. 5(b), the annealed sample displayed a near-band-edge emission (NBE) at the UV range and an evident broadband emission in the visible region at 535 nm. It can be inferred that annealing process caused more defects. The comparison of TRPL is shown in Fig. 5(c). It can be seen from Table I that $\tau_1$ decreases, $\tau_2$ increases, and $\varepsilon_{\tau 2}$ decreases, suggesting that the radiative recombination was dominant before annealing, while the UV emission process was modified by the nonradiative recombination centers of defect states generated in the bandgap for the annealed sample. It indicated that the effect of defect states in the carrier dynamics was enhanced after annealing. Therefore, it is reasonable to conclude that the increase in surface defects leads to a decrease in the efficiency of the transfer of trapped

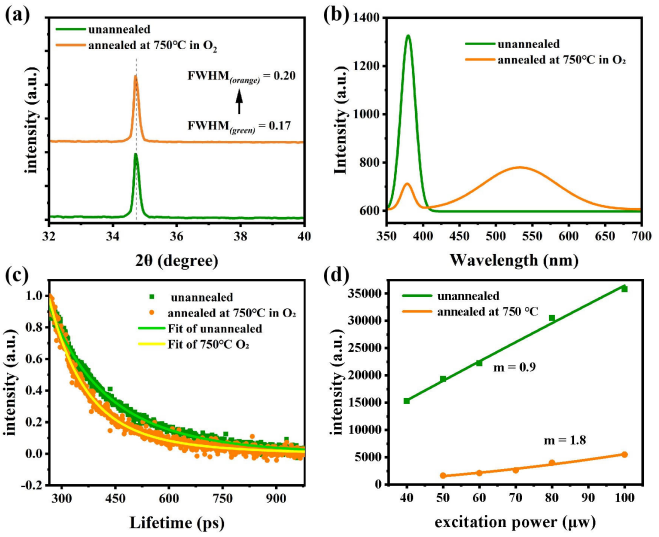


Fig. 5. Annealing treatment. (a) XRD pattern. (b) Room-temperature PL. (c) TRPL decay at 325 nm. (d) Variation of PL integrated intensity with the increasing of excitation power.

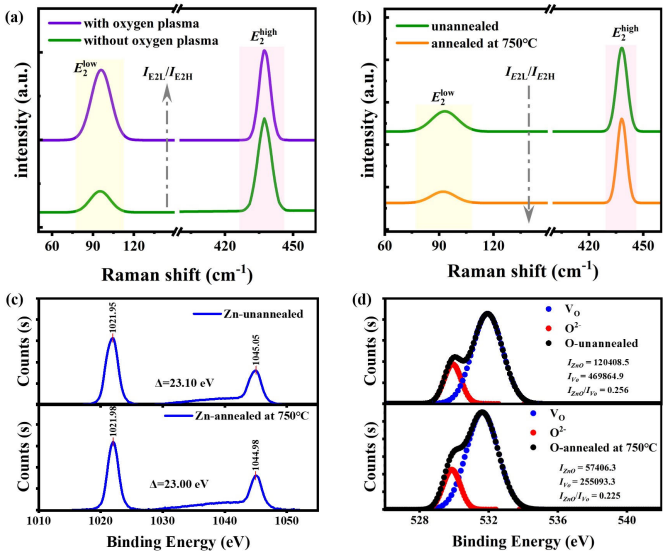


Fig. 6. Raman spectra for ZnO thin-film (a) oxygen plasma treatment and (b) annealing treatment. XPS spectra for ZnO thin film by annealing (c) Zn 2p core levels and (d) O core levels.

carriers back into the interior for efficient exciton emission. Fig. 5(d) shows the fitting results of the integral intensity and excitation power density by annealing. It can be obtained that m increases from 0.9 to 1.8, indicating that the emission of bound excitons caused by shallow-level defects is enhanced in the luminescence process, and the emission effect of intrinsic free excitons is relatively reduced. It further illustrated that the defect concentration of the ZnO thin film was increased after annealing.

The comparison of samples exhibited that NTC properties are related to the defect states of ZnO thin film. Then, Raman spectra of the ZnO thin films through oxygen plasma and annealing treatment are presented in Fig. 6(a) and (b). The two spectra display two mode peaks at 94 and 437 $cm^{-1}$, respectively. The intense Raman mode $E_2^{high}$ at 437 $cm^{-1}$

belongs to the oxygen vibration at high frequency, reflecting the lighter oxygen (anion) sublattice vibrations, while the $E_2^{low}$ mode at 94 $cm^{-1}$ is assigned to the vibration of the heavier zinc sublattice at low frequency, which is sensitive to the change of the zinc atom [28], [29]. After normalizing the peaks of the $E_2^{high}$ mode, it showed that the value of the relative vibration of the zinc sublattice ($I_{E2L}/I_{E2H}$) increased after oxygen plasma treatment while decreased after annealing. The increment and reduction of the $I_{E2L}/I_{E2H}$ as a result were in support of this proposal that it may be the $Zn_i$ that greatly affects the NTC properties of ZnO thin film.

Fig. 6(c) and (d) shows the XPS spectra of ZnO thin film annealed at 750 °C. The binding energy (BE) obtained in the XPS analysis was calibrated by referring the C 1 s at 284.5 eV in the standard manual. Fig. 6(c) depicts the two strong peaks at ~1021.8 and ~1044.8 eV of Zn $2p_{3/2}$ and Zn $2p_{1/2}$, respectively, confirming that zinc exists in the $Zn^{2+}$ state in the ZnO thin film. The energy difference (Δ) between the two Zn 2p peaks was 23.1 and 23 eV, which is in great agreement with the standard value of 22.97 eV. It can be observed that the Zn 2p peak shows a shift toward low BE after annealing, which may be due to the breaking of the Zn–O bond to generate oxygen-deficient Zn species ($Zn_i$) [30]. The O core-levels XPS spectra of ZnO thin film are given in Fig. 6(d). The O 1s spectra can be deconvoluted into two regions with peak binding energies at ~529.9 and ~531.9 eV. The lower BE at 529.91 and 529.86 eV is attributed to the oxygen ions in the fully oxidized Zn–O bond, while the higher BE at 531.93 and 531.63 eV is usually identified as the oxygen species adsorbed on the surface of ZnO [31]. The integrated intensities of the peak at ~529.9 eV of oxygen of the ZnO lattice ($I_{ZnO}$) and the peak at ~531.9 eV of the oxygen vacancy of the ZnO surface oxygen ($I_{VO}$) were obtained from Fig. 6(d). We calculated that the relative density of Zn–O bonds ($I_{ZnO}/I_{VO}$) decreased from 0.256 to 0.225 after annealing [32], which can further indicate that the Zn–O bonds of the annealed ZnO thin film were broken and the concentration of $Zn_i$ increased. It further demonstrated that $Zn_i$ plays an important role for the NTC response, which is reflected remarkably at the sensitivity properties of ZnO thin-film sensor.

In addition, the temperature-dependent PL spectra from 90 to 300 K were measured, as shown in Fig. 7. The intrinsic peak of ZnO film located at 380 nm is significantly red-shifted, while the non-intrinsic peak located at 540 nm is slightly blue-shifted. With the increase of temperature, the peaks are all broadened and the intensities generally show a decreasing trend. The temperature-dependent PL spectra of the ZnO intrinsic peak are displayed in Fig. 7(a). It can be found that the intensity decreases with increasing temperature from 90 to 150 K, while increases at 170 K and then returns to a decreasing trend from 170 to 300 K. Meanwhile, the intrinsic peak splits of 90–210 K. This may be due to the electron is captured by the shallow energy level ($Zn_i$), and then, the localized electron of $Zn_i$ is thermal-activated during the temperature change. From 90 to 150 K, the free excitons conduct radiation recombination transition and additional bound excitons act through the intermediate energy level states when the temperature increases, which is

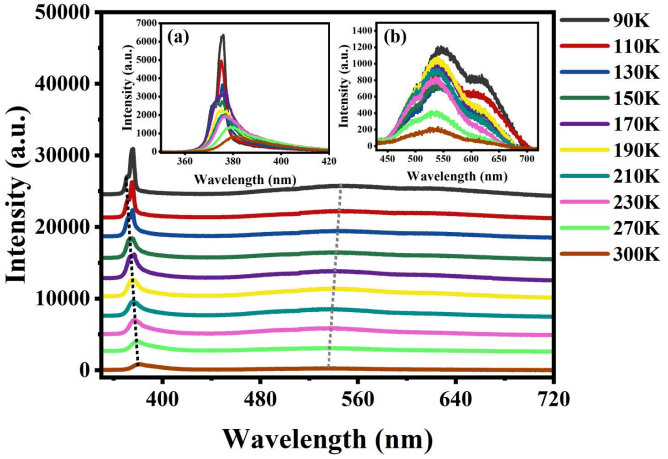


Fig. 7. Temperature-dependent PL spectra from 90 to 300 K for ZnO thin film. (a) ZnO intrinsic peak. (b) Nonintrinsic peak.

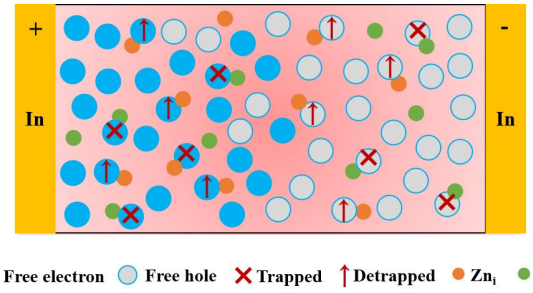


Fig. 8. Schematic of the mechanism of defects in ZnO thin-film temperature sensing.

the bound excitons localized in $Zn_i$ gain thermal energy to be activated to participate in the recombination transition, thus making the luminescence enhanced and causing the peak splitting phenomenon [33], [34], [35]. Here, the intermediate energy-level states are formed by shallow energy-level defects ($Zn_i$). The peaks of visible light originate from deep energy-level defects ($V_O$). As shown in Fig. 7(b), the position of the peak is slightly blue-shifted, which is probably due to the insufficient thermal energy provided by the temperature to fully activate the bound excitons localized at the deep energy level.

The sensor was designed based on the NTC property of ZnO thin film. The resistivity depends on the carrier dynamics behavior and the internal hindrance, where defects are one of the important components of it. As shown in Fig. 8, free electrons and holes migrate to electrodes under the action of the electric field, respectively. The high concentration of defects increases the probability of carrier trapping and more easily leads to electron–hole localization around the defects to form a high-resistance state. As the temperature changes, the trapped electron–hole gains thermal energy to be ionized and breaks free from shallow-level defects ($Zn_i$) to re-engage in carrier migration behavior. However, the carriers bound in deep energy level ($V_O$) are still heavily localized to maintain high-resistance states because of the insufficient activation of the thermal energy. When the value of temperature change ($\Delta T$) is the same, the higher the concentration of $Zn_i$, the greater the value of resistance change ($\Delta R$), which

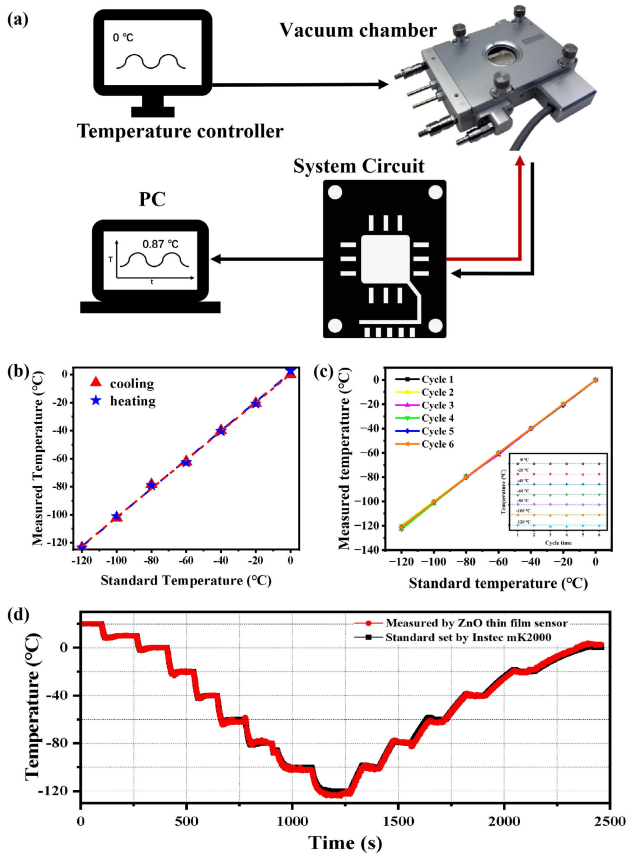


Fig. 9. (a) Schematic of ZnO thin-film temperature measurement platform. (b) Measured temperature and the standard temperature during the cooling and heating processes. (c) Temperature was recorded over six cycles. (d) Real-time temperature monitoring curve.

makes a higher NTC of ZnO thin film. Conversely, when the concentration of $Zn_i$ is less, the resistance change value ($\Delta R$) is smaller and the NTC of ZnO thin film is worse. Therefore, it can be concluded that $Zn_i$ is beneficial to improve the NTC response of ZnO thin-film sensor to some extent.

### D. Real-Time Temperature Monitoring for Simulated Cell Cryopreservation With ZnO NTC Sensor

Biomedical cryogenics applications strongly require the cryogenic monitoring with reliability, stability, and high sensitivity in long-term operation, such as samples cryopreservation, pharmaceutical storage, and transportation. Therefore, we simulated the application conditions of cell cryopreservation and conducted relevant tests in the common temperature range of −120 °C–0 °C. As shown in Fig. 9(a), a temperature measurement platform was constructed to verify the feasibility and reliability of ZnO thin-film NTC sensor. The ZnO thin film annealed at 750 °C with a good NTC response was placed in the vacuum chamber of the cooling-and-heating stage, whose temperature is set by the controller. The circuit system was designed for power supply and recording the resistance value to realize temperature visualization. In Fig. 9(b), the temperature was measured during heating and cooling process, respectively. The error between the measured and the set temperature is less than ±1.5 °C. It indicated the feasibility of ZnO low-temperature sensing. Moreover, the temperature was measured in several cycles, as shown in Fig. 9(c), and the value fluctuation was very small, which indicates the repeatability and recoverability of ZnO NTC sensor. The temperature monitored in real time is shown in Fig. 9(d). It showed that ZnO sensor had a fast response speed, which almost synchronizes with the commercial senso. The results proved the potential application of ZnO sensor for biomedical cryogenics in the future.

## IV. Conclusion

In summary, a low-temperature sensor was fabricated with slide ZnO thin film based on the experimentally proven NTC properties. The temperature-dependent $I$–$V$ characterizations were conducted, and the obtained $R$–$T$ results show a clear NTC response, which highly fitted with Boltzmann distribution. Oxygen plasma and annealing treatment were carried out to manipulate the defect states and catch their influence on NTC properties. The NTC response of ZnO thin film after oxygen plasma treatment became worse, while that of annealing treatment was improved. Then, XRD pattern, PL, and TRPL spectra were performed and compared for the cases before and after treatment, which suggested a correlation between defects and the NTC response. The mechanism of defect-related negative temperature response was studied by Raman, XPS, and temperature-dependent PL. The results demonstrated that $Zn_i$ played an important role on the NTC properties. Furthermore, we constructed the application environment of cell cryopreservation and conducted relevant tests in the common temperature range of −120 °C–0 °C. The real-time temperature was monitored with the ZnO NTC sensor, which showed a good feasibility, repeatability, and a fast response speed, which can almost synchronizes with the commercial low-temperature system. This study proved that ZnO NTC sensor is potential in biomedical cryogenics in the future. Meanwhile, it was concluded that defect manipulation is significant, which will contribute to the subsequent abundant and arduous researches of ZnO low-temperature sensing.

## References

[1] A. Youssefi et al., "A cryogenic electro-optic interconnect for superconducting devices," *Nature Electron.*, vol. 4, no. 5, pp. 326–332, May 2021, doi: 10.1038/s41928-021-00570-4.

[2] D. Ross-Pinnock and P. G. Maropoulos, "Review of industrial temperature measurement technologies and research priorities for the thermal characterisation of the factories of the future," *Proc. Inst. Mech. Eng. B, J. Eng. Manuf.*, vol. 230, no. 5, pp. 793–806, May 2016, doi: 10.1177/0954405414567929.

[3] A.-T. Buruiana et al., "Micrometer sized hexagonal chromium selenide flakes for cryogenic temperature sensors," *Sensors*, vol. 21, no. 23, p. 8084, Dec. 2021, doi: 10.3390/s21238084.

[4] J. Yang, B. Yin, X. Dong, W. Huang, and Y. Zou, "Ultrasensitive cryogenic temperature sensor based on a metalized optical fiber Fabry–Pérot interferometer," *J. Lightw. Technol.*, vol. 40, no. 16, pp. 5729–5735, Aug. 15, 2022, doi: 10.1109/JLT.2022.3181626.

[5] K. Blagg, P. Allen, T.-M. Lu, M. P. Lilly, and M. Singh, "Focused ion beam deposited carbon-platinum nanowires for cryogenic resistive thermometry," *Carbon*, vol. 169, pp. 482–487, Nov. 2020, doi: 10.1016/j.carbon.2020.06.087.

[6] E. A. Scott, A. Carow, D. Pete, and C. T. Harris, "Comparative analysis of the sensitivity of nanometallic thin film thermometers," *Nanotechnology*, vol. 33, no. 37, Sep. 2022, Art. no. 375503, doi: 10.1088/1361-6528/ac7650.

[7] V. L. Borblik, Y. M. Shwarts, and M. M. Shwarts, "Cryogenic diode thermometer insensitive completely to magnetic fields up to 1 T," *IEEE Sensors J.*, vol. 21, no. 4, pp. 4267–4271, Feb. 2021, doi: 10.1109/JSEN.2020.3031344.

[8] S. Chenghua, X. Juan, W. Helin, X. Tianning, Y. Bo, and L. Yuling, "Optical temperature sensor based on ZnO thin film's temperature-dependent optical properties," *Rev. Sci. Instrum.*, vol. 82, no. 8, Aug. 2011, Art. no. 084901, doi: 10.1063/1.3616361.

[9] A. Feteira, "Negative temperature coefficient resistance (NTCR) ceramic thermistors: An industrial perspective," *J. Amer. Ceram. Soc.*, vol. 92, no. 5, pp. 967–983, May 2009, doi: 10.1111/j.1551-2916.2009.02990.x.

[10] M. N. Muralidharan, E. K. Sunny, K. R. Dayas, A. Seema, and K. R. Resmi, "Optimization of process parameters for the production of Ni–Mn–Co–Fe based NTC chip thermistors through tape casting route," *J. Alloys Compounds*, vol. 509, no. 38, pp. 9363–9371, Sep. 2011, doi: 10.1016/j.jallcom.2011.07.037.

[11] C. Teichmann and J. Töpfer, "Sintering and electrical properties of Cu-substituted Zn-Co-Ni-Mn spinel ceramics for NTC thermistors thick films," *J. Eur. Ceram. Soc.*, vol. 42, no. 5, pp. 2261–2267, May 2022, doi: 10.1016/j.jeurceramsoc.2021.12.078.

[12] K. Park and J. K. Lee, "Mn–Ni–Co–Cu–Zn–O NTC thermistors with high thermal stability for low resistance applications," *Scripta Mater.*, vol. 57, no. 4, pp. 329–332, Aug. 2007, doi: 10.1016/j.scriptamat.2007.04.026.

[13] B. Li, Z. Li, D. Peng, L. Huang, S. Zhang, and H. Zhang, "Sb–doped ZnO ceramics: NTC thermistors with high temperature sensitivity and electrical stability," *J. Mater. Sci., Mater. Electron.*, vol. 32, no. 19, pp. 24296–24307, Oct. 2021, doi: 10.1007/s10854-021-06896-1.

[14] M. Que, C. Lin, J. Sun, L. Chen, X. Sun, and Y. Sun, "Progress in ZnO nanosensors," *Sensors*, vol. 21, no. 16, p. 5502, Aug. 2021, doi: 10.3390/s21165502.

[15] F. Xue, L. Zhang, W. Tang, C. Zhang, W. Du, and Z. L. Wang, "Piezotronic effect on ZnO nanowire film based temperature sensor," *ACS Appl. Mater. Interfaces*, vol. 6, no. 8, pp. 5955–5961, Apr. 2014, doi: 10.1021/am500993p.

[16] H. Wang, A. Yang, and L. Tang, "Wide measurement-range fiber-optic temperature sensor based on ZnO thin film," *Opt. Lasers Eng.*, vol. 60, pp. 49–53, Sep. 2014, doi: 10.1016/j.optlaseng.2014.03.008.

[17] S. A. Hasan et al., "ZnO thin film based flexible temperature sensor," in *Proc. IEEE SENSORS*, Glasgow, U.K., Oct. 2017, pp. 1–3, doi: 10.1109/ICSENS.2017.8234387.

[18] I. Ayoub et al., "Advances in ZnO: Manipulation of defects for enhancing their technological potentials," *Nanotechnol. Rev.*, vol. 11, no. 1, pp. 575–619, Jan. 2022, doi: 10.1515/ntrev-2022-0035.

[19] D. Smazna et al., "Buckminsterfullerene hybridized zinc oxide tetrapods: Defects and charge transfer induced optical and electrical response," *Nanoscale*, vol. 10, no. 21, pp. 10050–10062, 2018, doi: 10.1039/C8NR01504J.

[20] L. Cabral et al., "Insights into the nature of optically active defects of ZnO," *J. Lumin.*, vol. 227, Nov. 2020, Art. no. 117536, doi: 10.1016/j.jlumin.2020.117536.

[21] G. H. He et al., "Photodetectors for weak-signal detection fabricated from ZnO:(Li,N) films," *Appl. Surf. Sci.*, vol. 412, pp. 554–558, Aug. 2017, doi: 10.1016/j.apsusc.2017.03.295.

[22] B. Wang, J. Wang, J. Yao, and A. Chang, "Bismuth and zinc co-modified $Mn_{1.1}Co_{1.5}Fe_{0.4}O_4$ negative temperature coefficient sensitive ceramics: Structural and electrical characterization," *Mater. Chem. Phys.*, vol. 257, Jan. 2021, Art. no. 123604, doi: 10.1016/j.matchemphys.2020.123604.

[23] X. Sun, H. Zhang, Y. Liu, J. Guo, and Z. Li, "Characterization of new negative temperature coefficient thermistors based on Zn–Ni–O system," *J. Adv. Ceram.*, vol. 5, no. 4, pp. 329–336, Dec. 2016, doi: 10.1007/s40145-016-0206-0.

[24] B. Guo, Z. Ye, and K. S. Wong, "Time-resolved photoluminescence study of a ZnO thin film grown on a (100) silicon substrate," *J. Cryst. Growth*, vol. 253, no. 1, pp. 252–257, Jun. 2003, doi: 10.1016/S0022-0248(03)01006-6.

[25] Z. Zaaboub, F. Hassen, L. Chaabane, and H. Maaref, "Photoluminescence and time resolved photoluminescence properties in as grown ZnO thin films prepared by DC reactive sputtering for optoelectronic devices," *Microelectron. J.*, vol. 114, Aug. 2021, Art. no. 105153, doi: 10.1016/j.mejo.2021.105153.

[26] X. Zhang et al., "Improved photoluminescence quantum yield of $CsPbBr_3$ quantum dots glass ceramics," *J. Amer. Ceram. Soc.*, vol. 103, no. 9, pp. 5028–5035, Sep. 2020, doi: 10.1111/jace.17225.

[27] T. Schmidt, K. Lischka, and W. Zulehner, "Excitation-power dependence of the near-band-edge photoluminescence of semiconductors," *Phys. Rev. B, Condens. Matter*, vol. 45, no. 16, pp. 8989–8994, Apr. 1992, doi: 10.1103/PhysRevB.45.8989.

[28] J. M. Calleja and M. Cardona, "Resonant Raman scattering in ZnO," *Phys. Rev. B, Condens. Matter*, vol. 16, no. 8, pp. 3753–3761, Oct. 1977, doi: 10.1103/PhysRevB.16.3753.

[29] S. Horzum et al., "Monitoring the characteristic properties of Ga-doped ZnO by Raman spectroscopy and atomic scale calculations," *J. Mol. Struct.*, vol. 1180, pp. 505–511, Mar. 2019. Accessed: Mar. 8, 2023. [Online]. Available: https://www.zhangqiaokeyan.com/journal-foreign-detail/0704020707623.html

[30] M. Shaheera et al., "Characterization and device application of indium doped ZnO homojunction prepared by Rf magnetron sputtering," *Opt. Mater.*, vol. 101, Mar. 2020, Art. no. 109723, doi: 10.1016/j.optmat.2020.109723.

[31] W. Liu et al., "Thermal-assisted UV-photon irradiation to improve crystallization and luminescence efficiency of ZnO," *IEEE Trans. Electron Devices*, vol. 68, no. 7, pp. 3283–3289, Jul. 2021, doi: 10.1109/TED.2021.3077207.

[32] J. Yang, J. Lee, J. Lee, and W. Yi, "Oxygen annealing of the ZnO nanoparticle layer for the high-performance PbS colloidal quantum-dot photovoltaics," *J. Power Sources*, vol. 421, pp. 124–131, May 2019, doi: 10.1016/j.jpowsour.2019.03.013.

[33] M. Watanabe et al., "Negative thermal quenching of photoluminescence in ZnO," *Phys. B, Condens. Matter*, vols. 376–377, pp. 711–714, Apr. 2006, doi: 10.1016/j.physb.2005.12.178.

[34] X. Chen et al., "Negative thermal quenching of below-bandgap photoluminescence in InPBi," *Appl. Phys. Lett.*, vol. 110, no. 5, Jan. 2017, Art. no. 051903, doi: 10.1063/1.4975586.

[35] L. Lei et al., "Enhancing negative thermal quenching effect via low-valence doping in two-dimensional confined core-shell upconversion nanocrystals," *J. Mater. Chem. C*, vol. 6, no. 43, pp. 11587–11592, Nov. 2018, doi: 10.1039/C8TC04392B.